Research Square

Preprints are preliminary reports that have not undergone peer review.
They should not be considered conclusive, used to inform clinical practice,
or referenced by the media as validated information.

Contributions of climate and background mean-water level changes to storm surge inundation and damage under Typhoon Faxai in Tokyo Bay

Junbeom Jo

jbjo@jbnu.ac.kr

Jeonbuk National University

Nobuhito Mori

Kyoto University

Article

Keywords: Storm-surge inundation, Sea-level rise, Pseudo-global warming, Potential residential building damage, Shapley value, Non-additive effects

Posted Date: November 24th, 2026

DOI: https://doi.org/10.21203/rs.3.rs-11680168/v1

License: This work is licensed under a Creative Commons Attribution 4.0 International License.
Read Full License

Additional Declarations: No competing interests reported.

Contributions of climate and background mean-water level changes to storm surge inundation and damage under Typhoon Faxai in Tokyo Bay

Junbeom Jo [1,2*], Nobuhito Mori [2,3,4]

[1] Department of Civil Engineering, Jeonbuk National University, Jeonju 54896, Republic of Korea

[2] Disaster Prevention Research Institute, Kyoto University, Gokasho, Uji, Kyoto 611-0011, Japan

[3] Typhoon Science Technology Research Center, Yokohama National University, Yokohama 240-0067, Japan

[4] School of Engineering, Swansea University, Swansea SA1 8EN, UK

[*]**Corresponding author**: Junbeom Jo

Department of Civil Engineering, Jeonbuk National University

567 Baekje-daero, Deokjin-gu, Jeonju-si, Jeonbuk State 54896, Republic of Korea

Email: jbjo@jbnu.ac.kr

Abstract

Climate-conditioned inundation simulations are linked with established attribution methods in a framework for assessing factor contributions and non-additive damage. Applied to Typhoon Faxai (2019) in Tokyo Bay, it combines Weather Research and Forecasting (WRF) atmospheric fields with JAGURS-surge simulations under non-warming, present-day and +2 K and +4 K pseudo-global warming conditions. Potential residential building damage is evaluated using uniform exposure and a nonlinear depth-damage function. Sea-level rise (SLR) scenarios include a prescribed high-water level (HWL) increment of 1 m above mean sea level. Shapley values allocate total damage among drivers; Harsanyi decomposition identifies interaction effects. Combined damage reaches 709-891 billion JPY at +2 K and 898-1,180 billion JPY at +4 K. In +4 K experiments, damage beyond standalone sums represents 73-76% of total damage, or 44-48% when SLR and HWL are grouped. From lower to upper +4 K SLR, the SLR share increases from 23% to 32%, while storm forcing and HWL contributions rise in absolute terms despite declining shares. Between lower and upper SLR, 86-88% of additional damage occurs within previously inundated areas in both future climates, with storm forcing and HWL fixed. The framework supports coastal adaptation assessments of combined effects and damage intensification within existing inundated areas.

Keywords: Storm-surge inundation; Sea-level rise; Pseudo-global warming; Potential residential building damage; Shapley value; Non-additive effects

1 Introduction

Tropical cyclone storm surges threaten coastal populations and residential assets, while climate change alters mean sea level and storm characteristics [1, 2]. Global observations and reanalyses describe the distribution of surge hazards [3, 4], and projections show changes in extreme water levels and exceedance frequencies under warming [5, 6, 7]. Local impacts depend on storm size and track relative to coastal geometry and bathymetry [8]. Sea-level rise (SLR) reduces defense freeboard and alters inundation pathways, producing nonlinear responses and changing protection requirements [9, 10, 11]. Tide-surge interactions affect surge timing [12, 13], while SLR can modify regional tides [14]. Local assessments must therefore connect offshore water levels to land inundation and distinguish background levels from time-varying storm responses.

The pseudo-global warming (PGW) approach examines how observed storms respond to different climatic environments. Schär et al. [15] introduced thermodynamic modifications to regional model initial and boundary conditions, and Lackmann [16] applied this approach to Hurricane Sandy under past and future conditions. In Japan, d4PDF and its +2 K experiments provide climate perturbations for event-based assessments [17, 18]. Fujiwara et al. [19] found nonlinear changes in Typhoon Jebi intensity and structure under +2 K and +4 K warming. Fujiwara et al. [20] compared present-day, non-warming, and future conditions for Typhoon Hagibis using the same WRF configuration. Coupling such atmospheric fields to hydrodynamic models connects climatic changes to coastal responses. Li et al. [21] found spatially varying future surge increases along the Pearl River Delta coast and its estuaries. Storm intensity alone is consequently insufficient to describe local impacts in semi-enclosed bays such as Tokyo Bay.

Local inundation depends on interactions among flood drivers, so their combined effects cannot necessarily be represented by adding responses to individual drivers. Studies of surge and rainfall have examined joint occurrence in US coastal cities and future European climates [22, 23],

highlighting the dependencies central to compound hazard assessment [24]. Physical models have shown how elevated sea levels restrict drainage in Jakarta [25] and how storm tracks and river size affect the timing of surge and river flooding in Ise and Mikawa Bays [26]. For Typhoon Jebi at Kansai International Airport, Jo et al. [27] reproduced inundation depths more accurately with coupled coastal and pluvial simulations than by summing individual-process results. Recent simulations in Waikīkī also show how rising receiving-water levels can change the dominant flood sources [28]. These studies establish the importance of evaluating drivers together. However, a simulation with all drivers active does not itself distinguish their individual contributions or the additional response arising from their combination.

The damage associated with a given inundation pattern depends on the distribution and value of exposed assets and their vulnerability to flooding. Coastal loss estimates depend on exposed assets and protection levels as well as sea-level changes [29, 30]. Kwak et al. [31] likewise considered land-cover changes alongside event-specific weather in an urban flood assessment for Ulsan. Depth-damage methods connect these exposure assumptions to inundation severity [32, 33]. Applications include casualty and vehicle damage estimates in Macau [34] and building damage under perturbed typhoon tracks and levee heights in Japan [35]. An Irma-based assessment of Miami also identified nonlinear changes in affected population and economic damage under SLR scenarios [36]. In Tokyo Bay, Jo et al. [37] examined residential damage sensitivity to wind and pressure perturbations. Because equal inundated areas can have different depth distributions, area alone does not determine damage. Holding exposure and the damage function fixed provides a common basis for comparing damage responses to climate and water level conditions.

These findings motivate an assessment of how factor contributions and damage omitted by standalone assessments change across climate-specific sea-level projections. Contributions depend on the reference state used to evaluate a driver. Shapley [38] attribution addresses this dependence by averaging marginal effects over all orders of inclusion. Chowdhury et al. [39] applied all driver

combinations to quantify spatial and temporal contributions to compound flooding. Extending this analysis to damage requires the depth-damage function to be evaluated for each combination before attribution. Harsanyi [40] decomposition identifies the interaction terms within the resulting allocation, distinguishing contributions to total damage from the excess above standalone sums. Domain totals alone do not locate this additional damage. Relating them to newly inundated land and intensification within previously inundated areas clarifies whether rising sea levels mainly expand the affected area or deepen damage within it.

This study links PGW-based inundation and damage assessment with established Shapley attribution and Harsanyi decomposition to quantify factor contributions and non-additive damage in Tokyo Bay. WRF mean atmospheric fields for Typhoon Faxai (2019) drive JAGURS-surge under present-day, non-warming, and future climate conditions. Future experiments combine climate-specific SLR projections with a prescribed HWL. All combinations of TC, SLR, and HWL are evaluated under common exposure and damage assumptions. The analysis quantifies the excess of combined damage above standalone sums and compares relative and absolute factor contributions across SLR levels. To interpret the additional damage, it also separates inundation expansion from intensification within previously inundated areas. Together, these analyses characterize how SLR modifies damage under combined forcing and provide a basis for considering these responses in coastal adaptation assessments.

2 Study area and assessment methods

2.1 Study area

The study area comprises Tokyo Bay and the adjacent coastal lowlands in the Kanto region of Japan. Tokyo Bay is a semi-enclosed basin connected to the Pacific Ocean through its mouth, with Tokyo and Yokohama on the western side and Chiba on the eastern side. Bathymetry and coastal

geometry influence surge generation and propagation, whereas land topography and coastal defenses determine inundation pathways. Typhoon Faxai, which passed through the Kanto region in September 2019, was selected as the reference event. Surge residuals at Tokyo, Chiba, and Yokohama were used to evaluate the present-day simulation across the northern, eastern, and western bay. Inundation and potential residential damage were evaluated throughout the coastal land area represented in the innermost hydrodynamic domain.

2.2 WRF model and mean forcing fields

Typhoon atmospheric fields were generated using the Weather Research and Forecasting (WRF) model. The Advanced Research WRF dynamical core solves the compressible nonhydrostatic equations in terrain-following coordinates [41]. An initialization-time ensemble was constructed for each climate condition by starting simulations at different times. The climate perturbations and initialization times are specified in Section 3.2. At common valid times and coordinates, arithmetic means of the zonal and meridional 10 m wind components and sea-level pressure were calculated across the contributing members. Wind speed was obtained from the mean components rather than by averaging individual wind speed magnitudes. These mean wind and pressure fields were transferred to JAGURS-surge through one-way coupling. Hydrodynamic and damage responses were calculated from the mean forcing, not by averaging member-specific responses. This distinction defines the response assessed throughout the study.

2.3 JAGURS-surge and inundation metrics

Storm surge and inundation were simulated using JAGURS-surge [13], which incorporates atmospheric pressure and surface wind stress into JAGURS [42]. The depth-integrated nonlinear shallow water equations are written as follows.

$$\frac{\partial \eta}{\partial t} + \frac{\partial M}{\partial x} + \frac{\partial N}{\partial y} = 0 \tag{1}$$

$$\frac{\partial M}{\partial t} + \frac{\partial}{\partial x}\left(\frac{M^2}{D}\right) + \frac{\partial}{\partial y}\left(\frac{MN}{D}\right) - fN = -gD\frac{\partial \eta}{\partial x} - \frac{D}{\rho_w}\frac{\partial p_a}{\partial x} + \frac{1}{\rho_w}(\tau_{\mathrm{sx}} - \tau_{\mathrm{bx}}) \tag{2}$$

$$\frac{\partial N}{\partial t} + \frac{\partial}{\partial x}\left(\frac{MN}{D}\right) + \frac{\partial}{\partial y}\left(\frac{N^2}{D}\right) + fM = -gD\frac{\partial \eta}{\partial y} - \frac{D}{\rho_w}\frac{\partial p_a}{\partial y} + \frac{1}{\rho_w}\left(\tau_{\mathrm{sy}} - \tau_{\mathrm{by}}\right) \tag{3}$$

In Eqs. (1)-(3), t denotes time, and x and y are eastward and northward Cartesian coordinates. Water surface elevation is η, and M and N are depth-integrated discharges per unit width in the respective directions. Total water depth D is the sum of η and b, with b positive below the common vertical datum and negative on land above it. The symbols f, g, and ρ_w denote the Coriolis parameter, gravitational acceleration, and seawater density. Sea-level pressure is p_a. Surface shear stress components are τ_{sx} and τ_{sy}, while bottom shear stress components are τ_{bx} and τ_{by}.

Wind stress was calculated from the 10 m wind vector using the drag coefficient of Honda and Mitsuyasu [43], and bottom friction was represented using Manning roughness. The governing equations and stress formulations follow Jo et al. [13]. Coastal defenses were represented as linear structures at cell boundaries in the innermost grid using the implementation described by Jo et al. [37]. At each time step, the side with the higher water surface was defined as upstream. Flow across the boundary was blocked when the upstream water surface did not exceed the crest elevation. Once the crest was exceeded, overflow discharge per unit width was calculated using the free-overflow equation of Homma [44].

$$q_s = 0.35h_1\sqrt{2gh_1} \tag{4}$$

where q_s is overflow discharge per unit width and h_1 is the positive difference between the upstream water surface and the defense crest elevation. The calculated discharge was applied as the depth-integrated flux normal to the cell boundary, with its sign directed from upstream to downstream. This treatment controls flow between cells without raising the ground elevation of the entire cell containing a defense. Because downstream water level is not directly included in the free-overflow equation, discharge may be overestimated under submerged overflow. Defenses were assumed to remain intact, and structural failure and wave overtopping were not considered.

Inundation was aggregated over the initially dry land common to all experiments in the innermost domain. A fixed initial land mask allowed newly inundated areas under raised sea levels to be compared on the same basis. Maximum inundation depth in each cell was calculated as follows.

$$d_k = max(0, \eta_{max,k} + b_k) \quad (5)$$

where d_k is the maximum inundation depth in grid cell k, $\eta_{max,k}$ is the maximum water surface elevation recorded after spin-up, and b_k is the signed bed-depth variable defined above. Dry cells without a valid water surface elevation were assigned zero depth. Inundated area was calculated by summing the areas of cells with positive maximum depth within the analysis mask. A volume metric based on cellwise maximum depth was defined as follows.

$$V^* = \sum_k A_k \, d_k \quad (6)$$

In this expression, A_k is the area of grid cell k, and V^* combines inundation extent and maximum depth. Because maximum depths may occur at different times across cells, it does not represent the water volume present at a single instant.

2.4 Potential direct residential damage

Potential direct residential damage was calculated using inundation depth as hazard intensity, representative residential asset values as exposure, and depth-dependent damage ratios as vulnerability. The depth-damage approach follows Merz et al. [32] and Huizinga et al. [33], while the exposure constants were the same as those used by Jo et al. [37]. Building damage ratios and a floor height of 0.45 m above ground were adopted from the Japanese coastal project damage assessment guidelines [45]. Damage for each scenario was calculated as follows.

$$L = \sum_k A_k \, H \, F \, P \, r(d_k) \tag{7}$$

In Eq. (7), L is total potential direct residential damage, H is household density, F is mean residential floor area per household, and P is asset value per unit floor area. The damage ratio $r(d_k)$ is a function of maximum depth above ground.

Household density was 0.00349 households/m², mean floor area was 61.03 m²/household, and unit asset value was 61045 JPY/m². These constants were derived from official Tokyo Metropolitan Government and Ministry of Internal Affairs and Communications statistics [46, 47]. Density was calculated from Tokyo-wide household counts and area. Floor area represents newly constructed housing in the Tokyo wards in 2019, while unit value is the assessed building value from fixed asset statistics. The constants were held fixed to compare climate and water level responses under common residential exposure and vulnerability. They were applied throughout the initial land mask, including nonresidential land, without a residential land-use mask. The estimates therefore represent potential building damage under uniform residential asset assumptions, rather than actual housing losses or damage to port and industrial assets.

Table 1 gives the damage ratios by ground-referenced and floor-referenced depth. Dry cells had zero damage, whereas wet cells below the 0.45 m floor level had a ratio of 0.059. Above-floor classes began at ground-referenced depths of 0.45, 0.95, 1.45, and 2.45 m, with boundary values

assigned to the class beginning at that depth. Depths of at least 2.45 m incurred the full assigned building value. Floor height was a guideline-based assumption, not a building-specific measurement. Damage was evaluated separately for each driver combination before attribution. Household contents, industrial assets, public infrastructure, and indirect losses were excluded. For water level comparisons, cells changing from dry to wet were classified as newly inundated. Damage changes in cells already wet under the reference scenario were aggregated separately to distinguish expansion from intensification.

Table 1 Building damage ratios by inundation depth for a floor height of 0.45 m [45].

Depth above ground	Depth relative to floor	Damage ratio
Dry	—	0
Greater than 0 and less than 0.45 m	Below floor	0.059
0.45 to less than 0.95 m	Less than 0.5 m above floor	0.263
0.95 to less than 1.45 m	0.5-1 m above floor	0.391
1.45 to less than 2.45 m	1-2 m above floor	0.655
2.45 m or greater	2 m or greater above floor	1.000

2.5 Factor attribution and interaction analysis

The Shapley method averages the marginal contribution of each factor over all possible orders of inclusion [38]. Three factors were defined: tropical cyclone forcing (TC), sea-level rise (SLR), and prescribed high-water level (HWL). Shapley values were calculated independently for inundated area, the volume metric based on maximum depth, and potential direct residential damage. Their application to compound flood drivers follows Chowdhury et al. [39].

$$\varphi_i = \sum_{S \subseteq \mathcal{I} \setminus \{i\}} \frac{|S|!(n-|S|-1)!}{n!} [v(S \cup \{i\}) - v(S)] \quad (8)$$

where φ_i is the absolute contribution of factor i, $\mathcal{I}$ is the factor set, and n is its size (three here). The subset S excludes i, $|S|$ is its size, and $v(S)$ is the simulated area, volume metric, or damage for that combination. Relative contributions were defined as follows.

$$C_i = \frac{100\varphi_i}{v(\mathcal{I})-v(\emptyset)} \tag{9}$$

In Eq. (9), C_i is the relative contribution in percent, $v(\mathcal{I})$ is the response with all three factors present, and $v(\emptyset)$ is the no-factor baseline response.

No inundation occurred under the no-factor condition, giving a zero baseline. Absolute contributions were checked to sum to the total response and relative contributions to 100%. Both were compared because an absolute contribution can increase while its share declines. Attribution was calculated separately for each climate and SLR level. Experiments without SLR or HWL used the remaining two factors.

Harsanyi [40] decomposition was applied to relate fully combined damage to standalone responses.

$$\delta(S) = \sum_{R\subseteq S}(-1)^{|S|-|R|}v(R) \tag{10}$$

For this decomposition, $\delta(S)$ is the interaction term for combination S, R is a subset of S, and $|R|$ is its size. The response $v(R)$ denotes residential damage under that subset. With a zero baseline, first-order terms are standalone responses. Second-order terms are pairwise responses minus their standalone sums, and the pure third-order term is the full response after removing all first- and second-order terms. Each Shapley value includes interaction terms shared equally among the participating factors. Shapley analysis therefore allocates total contributions, whereas Harsanyi decomposition identifies the interactions within that allocation. Net non-additive damage was also calculated to compare the overall magnitude of the interaction effects.

$$L_{\text{int}} = v(\mathcal{I}) - \sum_{i\in\mathcal{I}} v(\{i\}) \tag{11}$$

In Eq. (11), L_{int} is the fully combined damage minus the sum of the three standalone damages. The symbol v denotes residential damage, and $v(\{i\})$ is damage with only factor i present.

Positive net non-additive damage indicates excess above standalone sums. Dividing it by fully combined damage gives the non-additive share. The sum of second- and third-order terms was checked against this excess. Sensitivity to factor grouping was examined by combining SLR and HWL into one background water level factor. Using the existing simulations, two-factor non-additive damage was calculated by subtracting TC-only damage and combined SLR-HWL damage from the full response.

3 Numerical experiments

3.1 Model configuration and simulation procedure

The WRF configuration of Fujiwara et al. [20] was applied to Faxai. WRF version 3.9.1.1 used two-way nesting between a 5 km outer domain and a 1 km inner domain, with 56 terrain-following vertical levels extending from the surface to 20 hPa. Initial and boundary conditions were obtained from the NCEP Final Operational Global Analysis (FNL) at 1° horizontal resolution. Cumulus parameterization was not used in either domain. Microphysics, boundary layer, surface, and radiation schemes followed that study. In the outer domain, spectral nudging was applied to horizontal winds above 750 hPa with zonal and meridional wavenumbers of 4 to constrain the synoptic flow. The same model configuration was used across climate conditions.

JAGURS-surge used four nested domains with grid spacings of 2430, 810, 270, and 90 m. Water levels calculated over the wider sea were transferred to the finer domains resolving Tokyo Bay and its coastal lowlands. The innermost domain contained 631×961 grid points. Manning roughness was 0.025 s $m^{-1/3}$ over water and land. Topography and coastal defenses were held fixed across

scenarios. The hydrodynamic time step was 0.5 s. Each 30 hr simulation began with a 12 h spin-up, during which forcing increased gradually from zero wind and uniform pressure of 1013 hPa to the first atmospheric input field. Land inundation was calculated only during the following 18 h, using atmospheric fields from 12:00 UTC on 8 September to 06:00 UTC on 9 September 2019. Forcing was interpolated linearly between 10 min inputs. Observational comparisons used this post-spin-up period. **Table 2** summarizes the numerical settings.

Table 2 Main numerical model settings.

Model	Parameter	Setting
Atmospheric	Model	WRF 3.9.1.1
	Grid and nesting	5 km and 1 km; two-way nesting
	Vertical levels and model top	56 levels; 20 hPa
	Initial and boundary fields	NCEP FNL 1°
	Cumulus parameterization	Not used
	Spectral nudging	Outer domain; horizontal winds above 750 hPa; wavenumber 4
Hydrodynamic	Model	JAGURS-surge
	Grid spacing	2430, 810, 270, 90 m
	Innermost domain	631×961 grid points; cell area 8100 m²
	Analysis area	433526 cells of common initial land
	Time step and duration	0.5 s; 12 h spin-up followed by 18 h atmospheric forcing
	Atmospheric input interval	10 min
	Manning roughness coefficient	0.025 s $m^{-1/3}$
	Vertical datum	Tokyo Peil (T.P.); reference water level 0 m

3.2 Climate conditions and tropical cyclone forcing

Climate experiments comprised present-day CTL, NAT with the historical warming component removed, and PGW2k and PGW4k corresponding to climates at +2 K and +4 K relative to preindustrial conditions. NAT follows a pseudo-non-warming approach. The future labels refer to warming levels in the climate datasets rather than spatially uniform increments applied to the Faxai field. We constructed perturbations in sea surface, surface air, and atmospheric temperatures from the d4PDF datasets [17, 18], following the procedure used by Fujiwara et al. [20]. These perturbations were applied to the initial and boundary conditions. Future temperature perturbations were based on differences between 30-year climatologies for 1981-2010 and 2051-2080. The non-warming condition was constructed by removing the difference between historical and non-warming climates. These thermodynamic modifications can be expressed as follows.

$$\begin{aligned} T_{PGW} &= T_{CTL} + \Delta T_{future} \\ T_{NAT} &= T_{CTL} - \Delta T_{historical} \end{aligned} \tag{12}$$

In Eq. (12), T_{CTL} is the present-day temperature field, while T_{PGW} and T_{NAT} are the future and non-warming fields. The monthly mean difference between future and present climates is ΔT_{future}, and $\Delta T_{historical}$ is the historical warming component.

Perturbations were constructed separately for sea surface, surface air, and atmospheric temperatures, with atmospheric perturbations varying vertically. Initial relative humidity was retained, and no separate climate perturbation was added to horizontal winds. This configuration allows the model to calculate the dynamical response to thermodynamic changes while limiting track displacement associated with external wind perturbations. Present-day mean sea level was retained for NAT, and future SLR was applied only to the two PGW conditions. NAT and CTL therefore compare non-warming and present-day atmospheric forcing at the same reference water level. The ensemble comprised 12 candidate initializations at 00:00, 06:00, 12:00, and 18:00 UTC on 5-7 September 2019. Outer-domain simulations ran from initialization to 06:00 UTC on 9 September. All

inner-domain simulations covered 12:00 UTC on 8 September to 06:00 UTC on 9 September. Mean fields were constructed as described in Section 2.2 and supplied to JAGURS-surge at 10 min intervals. Within each climate, the same forcing was retained while SLR and HWL varied.

3.3 Sea-level rise and prescribed high-water level

Future sea levels were based on projections for the Kanto coast, which includes Tokyo Bay, in the climate change report jointly published by the Ministry of Education, Culture, Sports, Science and Technology and the Japan Meteorological Agency [48]. The projections represent mean sea-level rise for 2081-2100 relative to 1986-2005. The central estimate and the endpoints of the likely range, spanning the 17th-83rd percentiles, were defined as central, lower, and upper SLR scenarios. PGW2k used lower, central, and upper levels of 0.30, 0.40, and 0.56 m, respectively. Corresponding PGW4k levels were 0.56, 0.68, and 0.88 m. SLR was applied as an increment above the common reference water level listed in **Table 2**. Combining atmospheric warming levels with end-of-century SLR defines event-based design scenarios for comparing the effects of those environmental conditions.

HWL was specified as a 1 m increment above mean sea level, following Jo et al. [13], who used a tidal amplitude of 1 m based on the Tokyo Bay design high water level of 0.97 m. Pickering et al. [14] reported small changes in tides at the representative Tokyo location under uniform SLR of 0.5-2 m in fixed-coastline experiments. The additional high water increment was therefore held at 1 m across climates as a common scenario assumption.

The background water level was raised by the prescribed SLR increment, with an additional 1 m in experiments with HWL. These static high water conditions replaced time-varying astronomical tides. SLR and HWL were treated as separate assessment factors to distinguish long-term mean sea-level change from high water superposition, although both raise the same background level in the

model. Their contributions therefore describe allocations associated with the prescribed increments. **Table 3** summarizes the climate and water level conditions.

Table 3 Numerical experiments by climate and water level condition.

Atmospheric forcing	SLR increment (m)	HWL increment (m)	No. of simulations
NAT	No SLR	0, 1	2
CTL	No SLR		2
PGW2k	No SLR lower (0.30) central (0.40) upper (0.56)		8
PGW4k	No SLR lower (0.56) central (0.68) upper (0.88)		8
No-TC	No SLR 0.30 0.40 0.56 0.68 0.88		12
Total	-	-	32

3.4 Experimental design and evaluation

For each SLR level in each future climate, the presence or absence of the three factors was crossed to form eight states. These comprised the no-factor baseline, three standalone states, three possible pairs, and the fully combined state. TC applies the wind and pressure fields of the corresponding climate together. No-TC experiments used zero wind and a spatially uniform pressure

of 1013 hPa. The TC contribution therefore represents the effect of adding the climate-specific typhoon to a No-TC state, rather than the warming increment relative to CTL.

Table 3 groups 32 simulated configurations by forcing and water level, including the verified zero-response baseline. NAT and CTL each used two water level conditions, and each PGW climate used eight. Twelve No-TC configurations covered the no-SLR condition and five distinct positive SLR levels, each with and without HWL. Runs shared by multiple factor combinations were reused across the six future climate-SLR cases. **Supplementary Table S1** lists these configurations, with the no-factor baseline included as the No-TC case without SLR or HWL. No-TC responses provided the reference for adding TC and for decomposing water level interactions.

Comparisons first examined the four atmospheric fields at present-day MSL, then combined HWL with the three SLR projections in each future climate. A comparison at the shared SLR of 0.56 m held background water level constant between future climates. Damage increases from lower to upper SLR were partitioned between newly and previously inundated cells at fixed forcing and HWL (Section 2.4). Attribution and interaction analysis covered each future climate and SLR level. Atmospheric evaluation distinguished outer-domain intensity extrema from local forcing at Tokyo meteorological station. Pressure and wind at Tokyo were compared with JMA observations, and modeled surge residuals with tide-gauge records over the common post-spin-up period. Atmospheric inputs at the three gauges provided further context for local water level responses.

4 Results and discussion

4.1 Model performance and atmospheric forcing

Present-day surge residuals were evaluated at Tokyo, Chiba, and Yokohama after astronomical tides were removed. Quantitative comparisons used 19 hourly observation-model pairs

346 from 12:00 UTC on 8 September to 06:00 UTC on 9 September 2019, excluding spin-up. Mean bias
347 was defined as model minus observation. **Figure 1** compares the time series, and **Table 4** reports
348 performance metrics. RMSE values were 0.19, 0.16, and 0.17 m, respectively. Chiba had the highest
349 correlation (0.954), and station mean biases ranged from −0.07 to +0.01 m. The modeled rise and
350 decline broadly followed observations, although peak differences remained. The modeled peak at
351 Tokyo of 0.94 m was 0.11 m below observations and approximately 27 min early. Peak
352 underestimates at Chiba and Yokohama were 0.18 and 0.16 m. Yokohama also had a timing
353 difference of approximately 3 h 10 min. Timing comparisons at Chiba and Yokohama were limited
354 by hourly observations. These discrepancies qualify the representation of local peaks. Agreement in
355 bay water levels does not validate inundation depths or building damage on land, particularly where
356 excluded wave overtopping may contribute.

357

Table 4 CTL performance against observations.

Variable	Station	Unit	Samples	RMSE	Mean bias	Correlation
Surge residual	Tokyo	m	19	0.19	-0.070	0.823
	Chiba	m	19	0.16	+0.007	0.954
	Yokohama	m	19	0.17	-0.027	0.773
Sea-level pressure	Tokyo	hPa	109	3.11	−1.47	0.990
Wind speed	Tokyo	m/s	109	3.33	+2.26	0.808

358

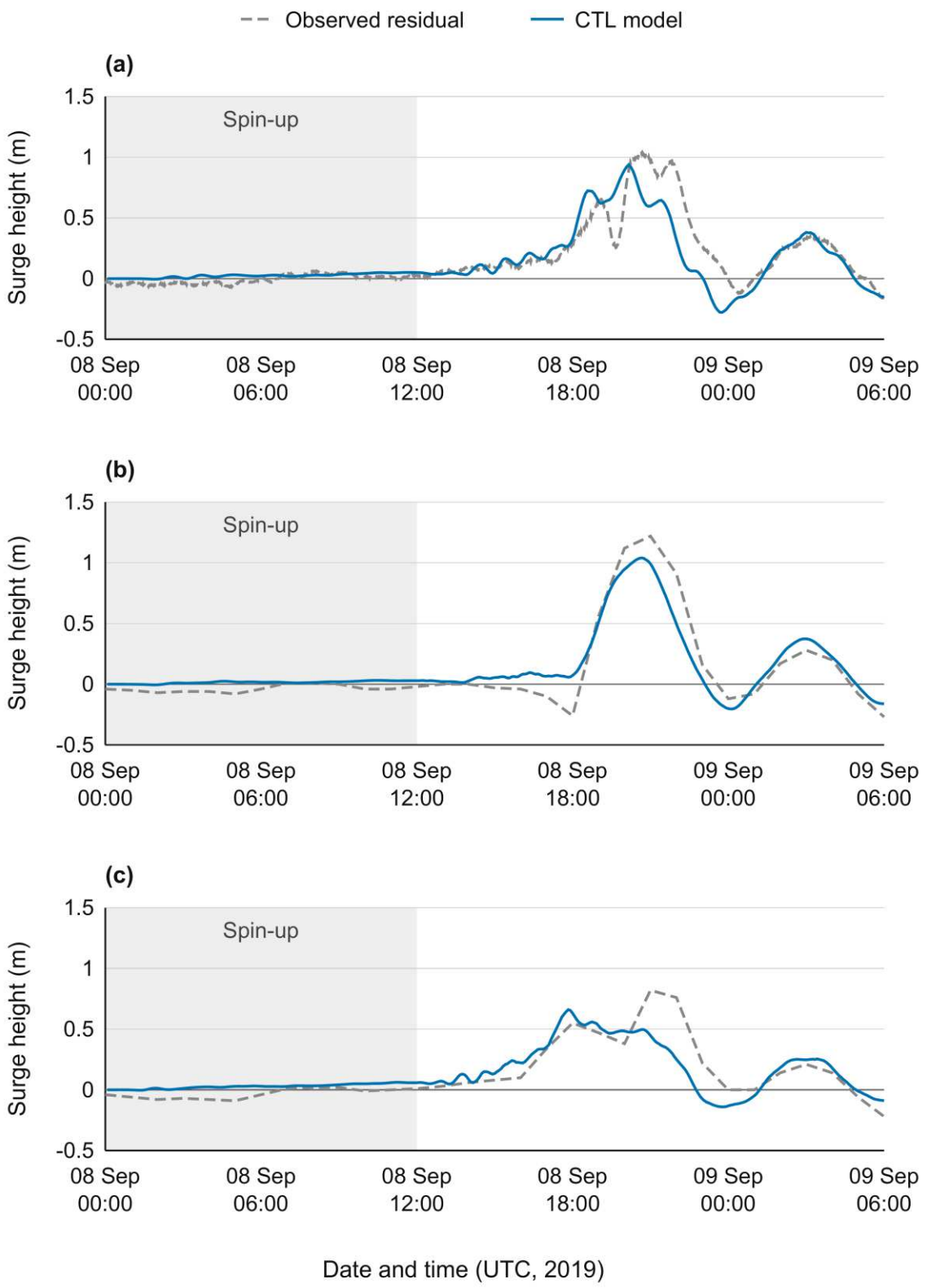

Fig. 1 Observed and control run (CTL) surge residuals at (a) Tokyo, (b) Chiba, and (c) Yokohama. Gray dashed lines denote observations, blue solid lines denote CTL, and shading indicates spin-up.

359

Figure 2(a, b) compares minimum sea-level pressure and maximum 10 m wind speed in the outer-domain mean fields at the same 19 hourly times. Minimum pressures were 956.42, 951.67, 938.21, and 921.80 hPa for NAT, CTL, PGW2k, and PGW4k. Maximum winds were 39.92, 44.98, 52.03, and 65.58 m/s. Both future fields were more intense than CTL. JMA best-track curves describe the intensity evolution of the observed event [49]. However, domain extrema need not coincide with the storm center and were not treated as direct estimates of central intensity error. **Figure 2(c, d)** compares hydrodynamic inputs at Tokyo meteorological station with 109 JMA observation pairs at 10 min intervals [50]. Observed winds are temporal means, while modeled winds are magnitudes of ensemble mean vectors. Differences in measurement height and averaging affect this comparison. CTL reproduced the pressure decline and recovery with correlation 0.990 and RMSE 3.11 hPa (**Table 4**). Its minimum was 973.14 hPa versus 980.00 hPa observed, occurring 10 min later. Wind agreement was weaker, with a correlation of 0.808 and an RMSE of 3.33 m/s. The modeled maximum of 19.37 m/s exceeded the observed 15.40 m/s and occurred approximately 1 h 30 min earlier. Local forcing did not follow the domain intensity ranking. At Tokyo, PGW2k minimum pressure and maximum wind were 967.84 hPa and 25.12 m/s, compared with 973.43 hPa and 25.46 m/s for PGW4k (**Fig. 2(c, d)**). PGW2k thus produced the larger local pressure drop despite the lower domain minimum pressure of PGW4k.

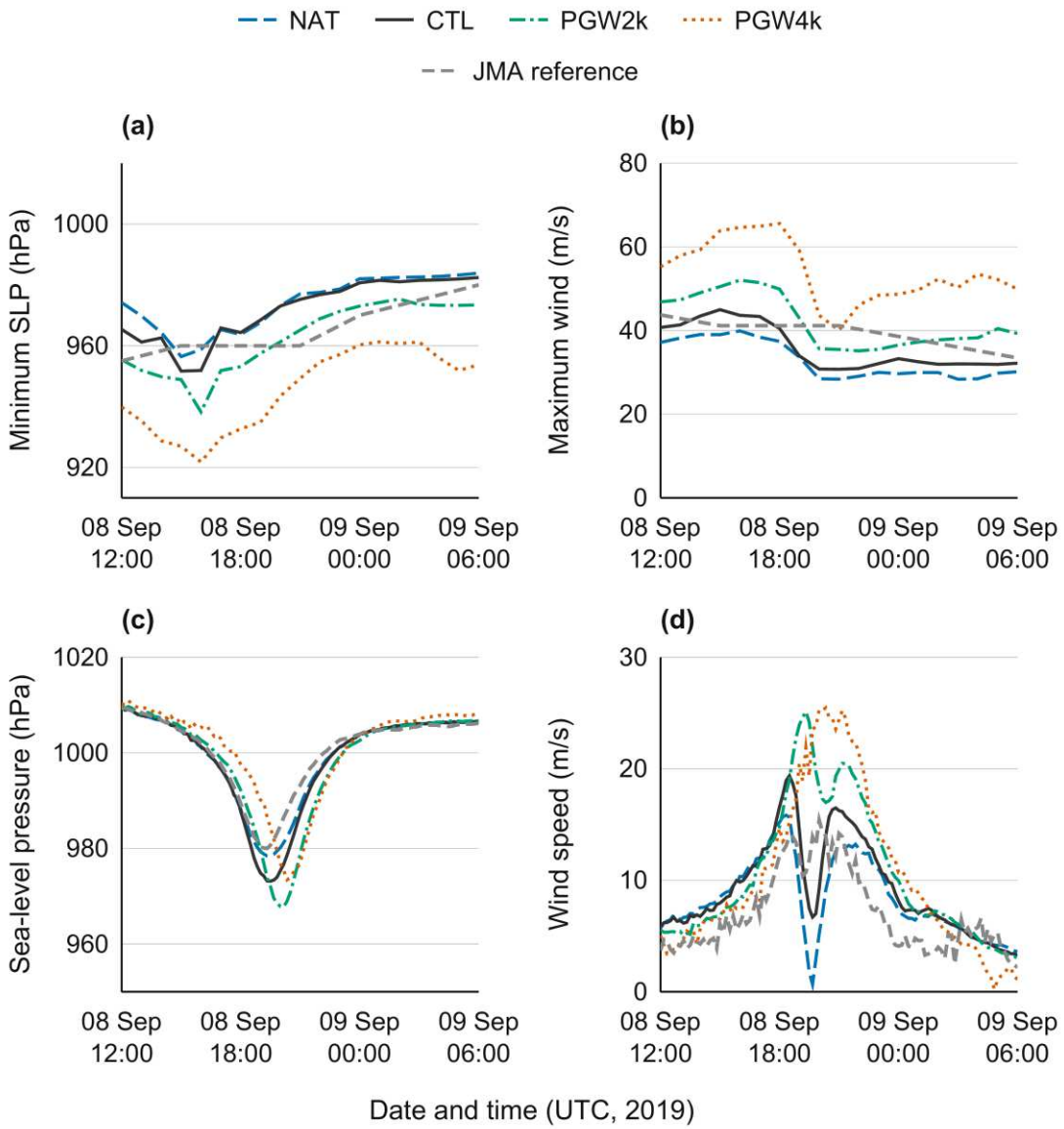

Fig. 2 Atmospheric fields across climates and JMA reference data. (a, b) Minimum sea-level pressure and maximum 10 m wind speed in the outer WRF domain and (c, d) sea-level pressure and wind speed at Tokyo meteorological station. Gray dashed lines denote JMA best-track data in (a, b) and station observations in (c, d).

377

378 **Figure 3** compares minimum-pressure paths in the mean fields with the JMA best track. Near
379 Tokyo Bay, the PGW4k path lies east of the NAT and CTL paths. This provides spatial context,
380 although the paths alone do not separate track effects from intensity and structure changes. Pressure
381 and wind at Tokyo, Chiba, and Yokohama tide gauges also differed in magnitude and timing

(**Supplementary Fig. S1**). The domain extrema describe the wider storm, whereas these fixed-point series show the forcing applied near the coast. Their differing rankings help explain why stronger domain-scale winds and lower pressures need not produce the highest water level at every station. Consistent with these differences in local forcing, water level rankings also varied across the bay. Tokyo peaks were 0.79, 0.94, 1.20, and 0.92 m for NAT, CTL, PGW2k, and PGW4k. Yokohama peaks were 0.58, 0.66, 0.99, and 1.16 m, with the highest under PGW4k. Chiba peaks were 0.93, 1.04, 1.36, and 1.35 m, giving similar values for the two future conditions. These differences connect the local forcing patterns to the hydrodynamic response. Li et al. [21] likewise found spatially varying future surge increases along coasts and estuaries. Domain-scale storm intensification therefore needs to be interpreted through the forcing acting on each part of the bay when assessing future inundation.

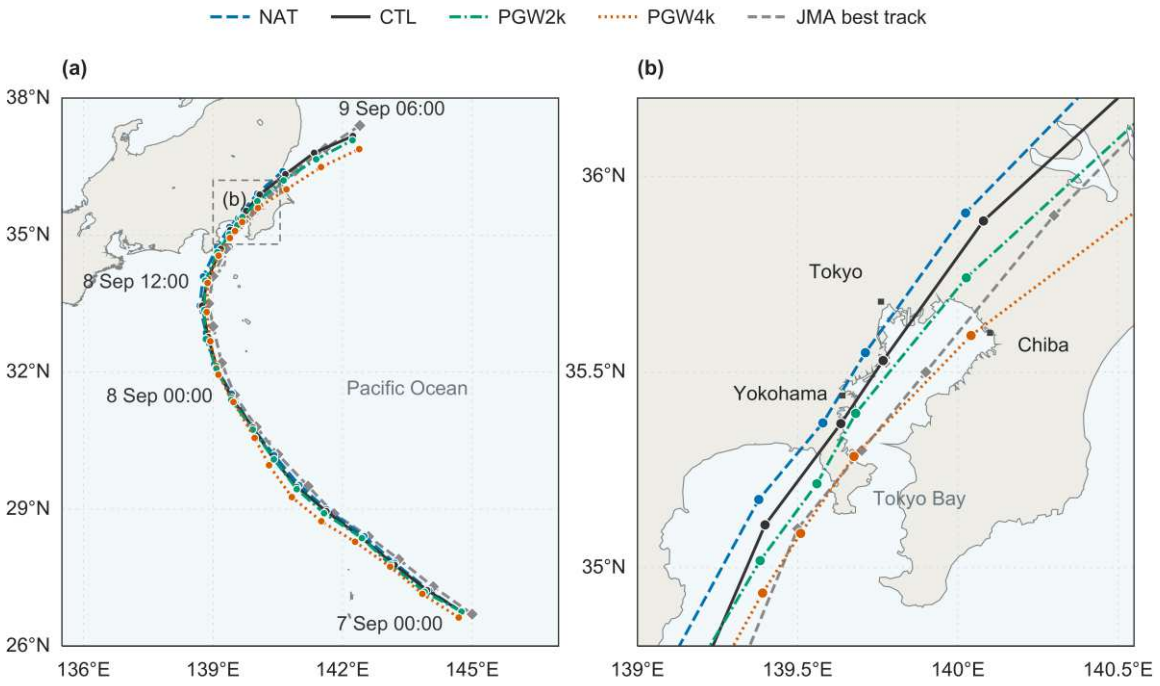

Fig. 3 Tracks of modeled minimum sea-level pressure and the JMA best-track data. (a) Regional overview and (b) Tokyo Bay enlargement. Circles denote model positions and diamonds denote JMA positions from 00:00 UTC on 7 September to 06:00 UTC on 9 September 2019.

4.2 Inundation response to climate and water level changes

Table 5 presents inundated area and the maximum-depth-based volume metric (V^*), together with potential direct residential damage for all main experiments with TC forcing. At MSL, inundated areas were 23.66, 26.71, 39.34, and 42.07 km² for NAT, CTL, PGW2k, and PGW4k, respectively. The two future areas were 47.3% and 57.5% larger than CTL. V^* increased from 10.62×10^6 m³ in CTL to 20.16×10^6 m³ in PGW2k and 21.63×10^6 m³ in PGW4k. The larger proportional increase in V^* than in area indicates that the applied future mean fields increased maximum depths as well as inundation extent. Differences among climates describe responses to the mean forcing constructed for each condition and therefore include the effects of warming, member selection, and track differences.

Figure 4 shows spatially uneven inundation in PGW2k that expands and deepens as SLR increases. Without HWL, inundated areas were 64.74, 72.43, and 85.07 km² under lower, central, and upper SLR. Adding HWL increased these areas to 143.25, 151.80, and 166.02 km². At central SLR, the inundated area was approximately 2.10 times that without HWL (**Fig. 4(b, e)**). This increase occurred under the same atmospheric forcing and SLR, demonstrating the influence of the prescribed high-water increment. The maps also show that the response varies along the coast with terrain and defense conditions. **Figure 5** presents the same comparison for PGW4k. Lower, central, and upper SLR without HWL produced inundated areas of 86.18, 94.63, and 110.27 km² (**Fig. 5(a-c)**). With HWL, these increased to 166.84, 175.85, and 193.04 km² (**Fig. 5(d-f)**). Upper SLR combined with HWL produced the largest area and V^* among the future experiments (**Fig. 5(f)**). In both climates, adding HWL at a fixed SLR level widened the inundated coastal zone and increased the extent of deep inundation. This response reflects changes in water surface elevation relative to the terrain and defense crests as the background level rises.

Table 5 Inundation and potential direct residential damage by climate and water level condition.

Climate	SLR level	HWL	Area (km^2)	V^* (10^6 m^3)	Damage (billion JPY)
NAT	Present-day MSL	Without	23.66	8.67	39.86
		With	93.73	78.27	354.75
CTL	Present-day MSL	Without	26.71	10.62	48.61
		With	98.93	83.68	382.13
PGW2k	Present-day MSL	Without	39.34	20.16	92.32
		With	118.18	111.59	510.99
	Lower	Without	64.74	39.90	181.46
		With	143.25	156.30	709.38
	Central	Without	72.43	48.39	219.69
		With	151.80	172.16	775.42
	Upper	Without	85.07	63.17	287.87
		With	166.02	200.58	891.36
PGW4k	Present-day MSL	Without	42.07	21.63	99.37
		With	120.29	112.40	514.68
	Lower	Without	86.18	64.68	292.82
		With	166.84	201.11	897.50
	Central	Without	94.63	76.10	347.11
		With	175.85	222.83	993.24
	Upper	Without	110.27	97.33	447.91
		With	193.04	263.78	1179.79

418

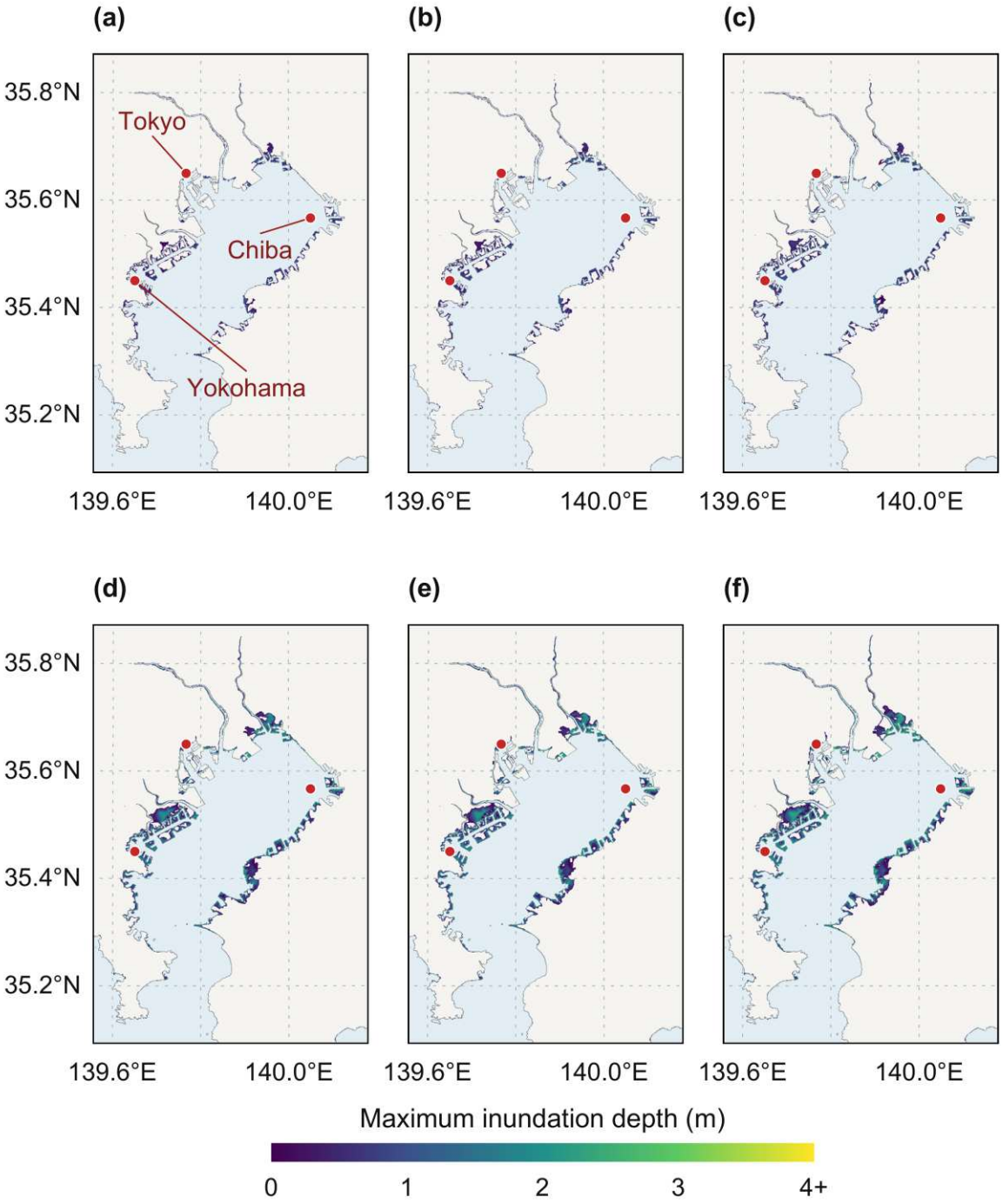

Fig. 4 Maximum inundation depth for PGW2k. (a-c) Without HWL and (d-f) with HWL. Columns show lower (0.30 m), central (0.40 m), and upper (0.56 m) SLR from left to right. Red circles indicate tide gauges.

419

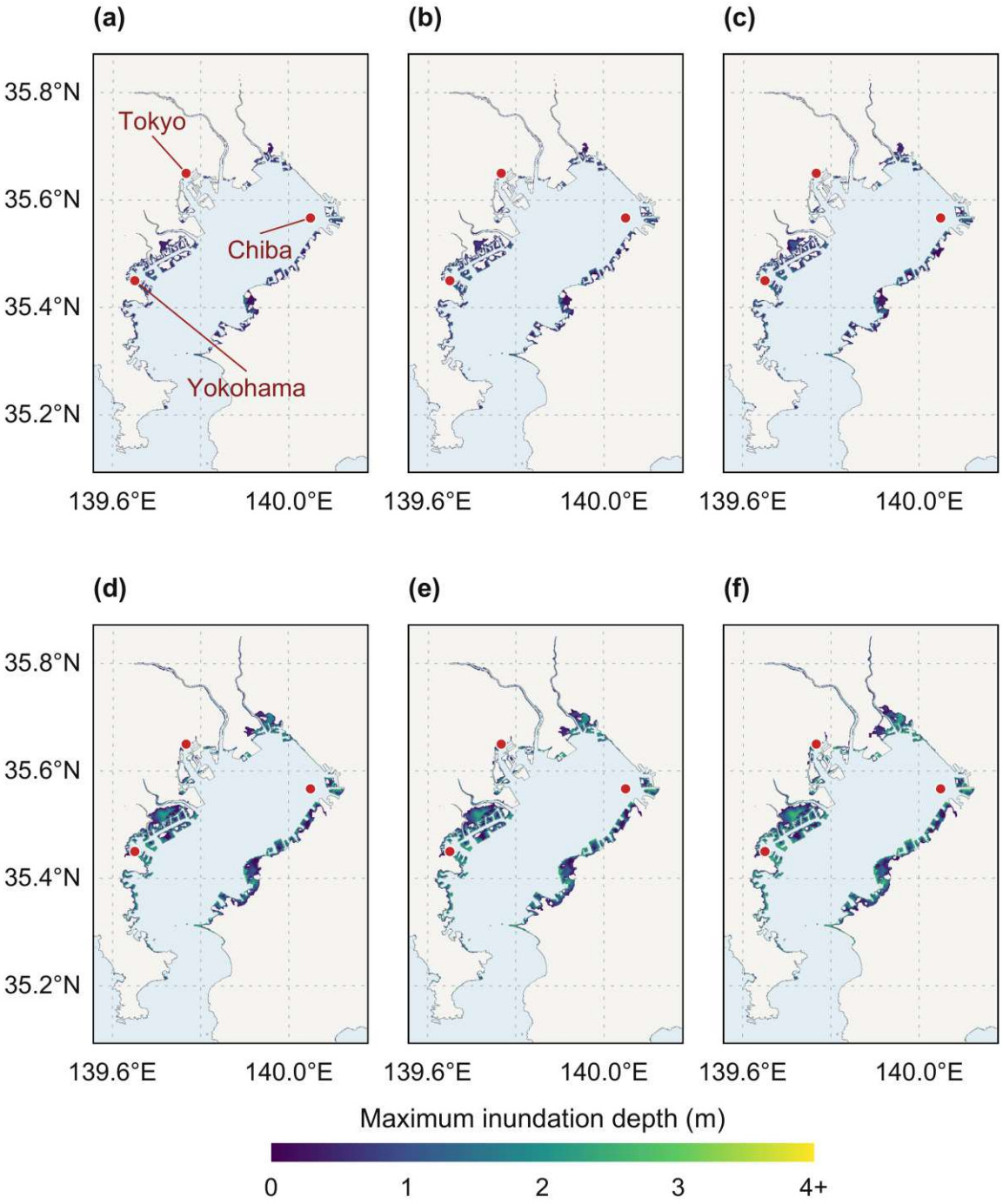

Fig. 5 Maximum inundation depth for PGW4k. (a-c) Without HWL and (d-f) with HWL. Columns show lower (0.56 m), central (0.68 m), and upper (0.88 m) SLR from left to right. Red circles indicate tide gauges.

420

The HWL-only condition, with a 1 m increment but no TC or SLR, also produced 51.27 km² of inundation (**Supplementary Table S1**). **Supplementary Fig. S2** overlays maximum depths for this condition with the defense distribution represented in the model. Inundation was unevenly distributed along the bay. The eastern enlargement also shows inundation on land seaward of defense lines located inland from the coastline (**Supplementary Fig. S2**). This arrangement provides spatial context for distinguishing some No-TC inundation from flooding behind coastal defenses. The overlay of maximum depth and defense location alone, however, does not identify individual inflow pathways.

The increase in inundation extent and depth with background water level shows why future impacts cannot be compared using climate-specific storm intensity alone. A supporting comparison at the common SLR level of 0.56 m gave small differences in aggregate inundation between the two future climates (**Supplementary Table S2**). Relative differences in that table use PGW2k as the reference. Comparisons using the projected sea level for each climate incorporate changes in both atmospheric forcing and sea level and therefore cannot be attributed solely to storm intensification. Crossing atmospheric forcing with background water level distinguishes these conditions and quantifies how changing water level modifies inundation extent and depth under the same forcing. The joint changes in extent and depth are consistent with the nonlinear sea-level responses examined by Bilskie et al. [9]. They also complement assessments of changing protection design heights [10], although the present experiments retain fixed terrain and defenses and use prescribed HWL. Across this controlled set of conditions, similar aggregate inundation does not ensure similar local depths. The maps therefore provide information about the distribution of inundation that is not captured by domain totals alone.

4.3 Potential residential damage and depth effects

At MSL, potential direct residential damage was 39.86, 48.61, 92.32, and 99.37 billion JPY for NAT, CTL, PGW2k, and PGW4k, respectively (**Table 5**). Relative to CTL, future damage increased by 89.9% and 104.4%, exceeding the corresponding increases in inundated area. Because all experiments used the same exposure constants and damage function, this difference reflects both inundation expansion and shifts toward depth classes with higher damage ratios. With future SLR and HWL combined, damage ranged from 709.38 to 891.36 billion JPY across the lower to upper PGW2k scenarios and from 897.50 to 1179.79 billion JPY for PGW4k. At the central SLR levels, HWL increased damage by factors of approximately 3.53 and 2.86 relative to conditions without HWL. The larger proportional increase in damage than in area indicates that higher water levels both inundated additional land and moved already inundated locations into higher damage classes. Scenario damage values are presented in **Table 5**, and the two future climates at common SLR are compared in **Supplementary Table S2**.

Figure 6 partitions PGW2k and PGW4k damage with HWL into the five depth classes in **Table 1**. Total bar height represents damage, while the segments show its depth composition. In PGW2k, the damage share from ground-referenced depths of at least 2.45 m, where the full assigned building value is counted as damage, increased from 2.4% at lower SLR to 4.1% at central SLR and 8.1% at upper SLR (**Fig. 6(a)**). Corresponding PGW4k shares were 9.4%, 14.7%, and 25.5% (**Fig. 6(b)**). Rising background levels therefore changed both total damage and its distribution among severity classes.

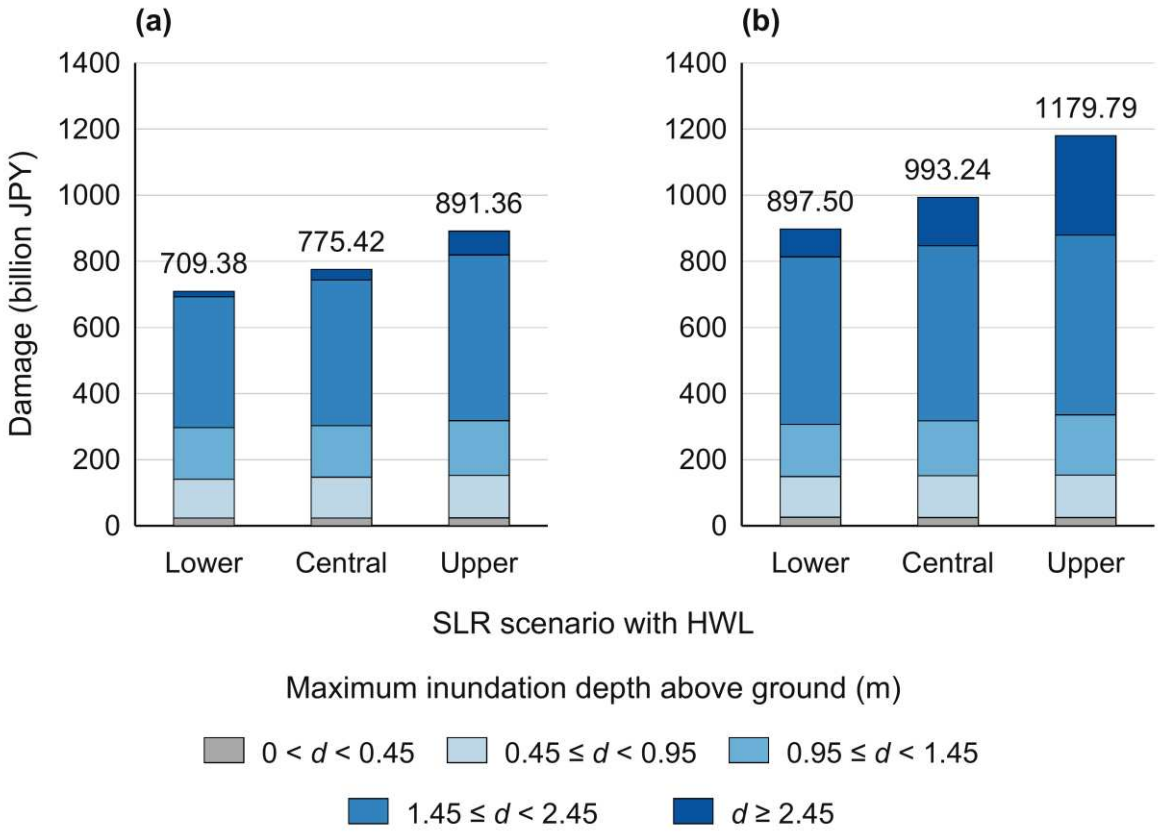

Fig. 6 Potential residential building damage by depth class with HWL for (a) PGW2k and (b) PGW4k. d denotes maximum inundation depth above ground.

464

465 Damage increases from lower to upper SLR were compared cell by cell while keeping
466 atmospheric forcing and HWL fixed. For PGW2k, damage in newly inundated cells accounted for
467 25.15 billion JPY of the total increase of 181.98 billion JPY. Damage increases in previously
468 inundated cells accounted for 156.83 billion JPY, or 86.18%. For PGW4k, newly inundated cells
469 contributed 33.95 billion JPY of the total increase of 282.29 billion JPY, while increases in
470 previously inundated cells contributed 248.34 billion JPY, or 87.97%. Newly inundated areas were
471 22.77 and 26.20 km² for PGW2k and PGW4k, respectively. No previously inundated cell shifted to a
472 lower damage class in either comparison. Areas of previously inundated land shifting to higher
473 damage classes were 57.49 and 83.79 km². Additional damage over the examined SLR range

474 therefore arose mainly from intensification within previously inundated areas rather than from the
475 newly inundated extent. This comparison uses cellwise maximum depths, which can occur at
476 different times.

477 The spatial partition identifies damage increases that an area-based assessment would miss.
478 Under the depth-damage relationships in **Table 1**, rising water levels moved previously inundated
479 cells into higher damage classes. The resulting dominance of intensification reflects both the
480 simulated depths and the assigned vulnerability under uniform exposure. Damage estimates depend
481 on these assumptions [32, 33], so the proportions describe the examined SLR range rather than a
482 general ratio for other coasts or asset distributions.

483

484 **4.4 Relative and absolute factor contributions**

485 Three-factor attribution focused on the two future climates at each SLR level. **Figure 7**
486 compares relative contributions to inundated area, V^*, and residential damage, using Eq. (8) for
487 absolute contributions and Eq. (9) for percentages. Each bar sums to 100%. In PGW2k, the SLR
488 damage share increased from 14.52% at lower SLR to 18.05% at central SLR and 23.54% at upper
489 SLR, while TC decreased from 39.98% to 35.27% and HWL from 45.50% to 41.19% (**Fig. 7(c)**).
490 PGW4k showed the same pattern. SLR shares were 23.43%, 26.97%, and 31.96%, while TC
491 decreased from 35.68% to 31.27% and HWL from 40.89% to 36.77% (**Fig. 7(f)**). HWL had the
492 largest damage share in all conditions. At upper PGW4k SLR, the SLR share slightly exceeded that
493 of TC. This ordering depends on the prescribed 1 m HWL, the selected SLR increments, and the
494 damage function.

495

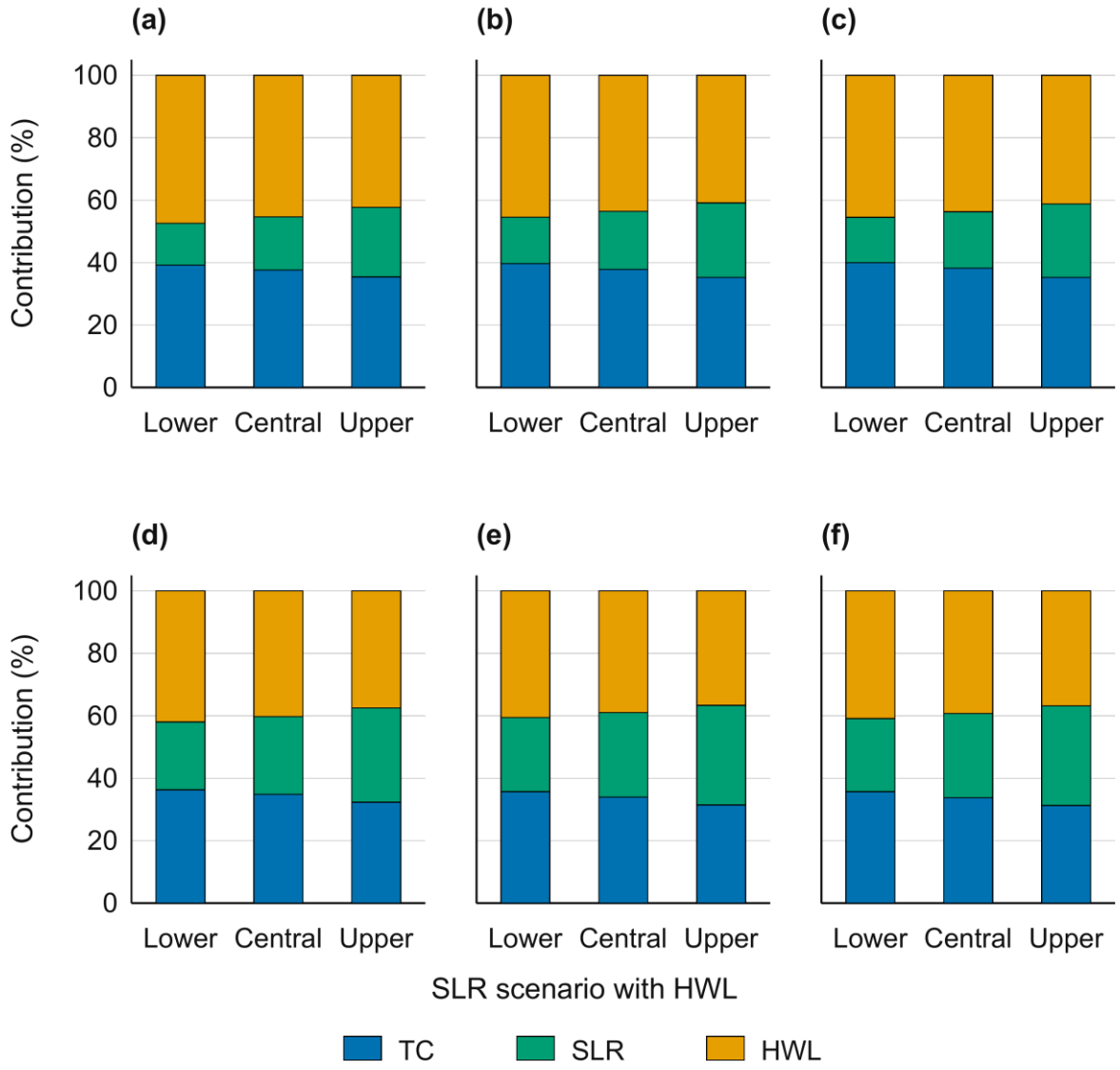

Fig. 7 Relative contributions of TC, SLR and HWL to inundation and residential damage for (a-c) PGW2k and (d-f) PGW4k. Columns show inundated area, the maximum-depth-based volume metric, and residential damage from left to right.

496

497 **Figure 8** presents absolute damage Shapley values for PGW2k and PGW4k, calculated by
498 applying Eq. (8) to damage. Unlike the relative contributions in **Fig. 7(c, f)**, each bar allocates the
499 total damage in **Fig. 6** among the three factors. From lower to upper PGW4k SLR, TC contributions
500 increased from 320.20 to 368.91 billion JPY, SLR from 210.32 to 377.04 billion JPY, and HWL from

366.98 to 433.84 billion JPY. Each colored segment therefore grows in absolute magnitude in **Fig. 8(b)**, even though TC and HWL occupy smaller percentages in **Fig. 7(f)**. Interpreting a declining share as a reduction in damage influence would miss this absolute increase. Comparing both measures separates changes in allocation from changes in damage magnitude and avoids judging the importance of a driver solely by its relative ranking.

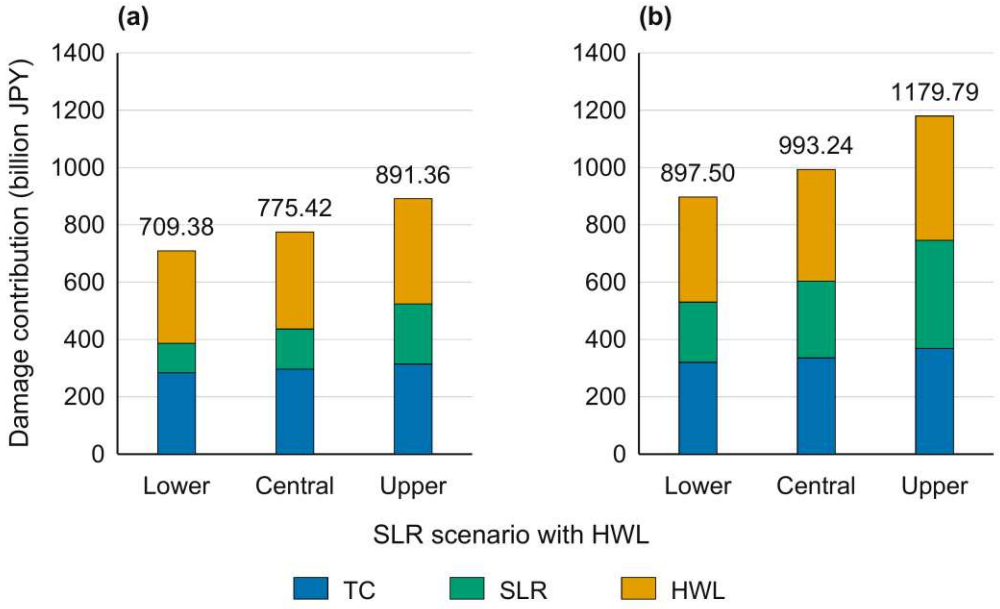

Fig. 8 Absolute contributions of TC, SLR and HWL to residential damage for (a) PGW2k and (b) PGW4k.

The contributions to area, V^*, and damage had similar overall structures but differed in magnitude. At lower PGW4k SLR, the SLR shares were 21.76% for area, 23.78% for V^*, and 23.43% for damage. At upper SLR, they were 30.14%, 31.90%, and 31.96%, respectively (**Fig. 7(d-f)**). These differences of up to about two percentage points show that allocation depends on whether the response measures extent, weights maximum depth, or applies a damage function. The damage function did not substantially reorder the factors in this case. Nevertheless, attribution needed to be calculated from damage rather than transferred directly from physical inundation metrics.

Chowdhury et al. [39] applied Shapley analysis to contributions to compound flood water levels. Here, applying it to potential residential damage reveals increasing absolute contributions that declining percentages alone would obscure. This allocation includes interactions shared among the participating factors. In particular, the HWL contribution is neither HWL-only damage nor an occurrence probability for actual tides. It describes the contribution of the prescribed water level increment under the specified combinations.

4.5 Non-additive damage and adaptation implications

Table 6 compares fully combined damage with standalone sums using Eq. (11). At central PGW4k SLR, total damage was 993.24 billion JPY and the standalone sum was 254.19 billion JPY, leaving net non-additive damage of 739.05 billion JPY, or 74.41%. Shares at lower and upper SLR were 73.33% and 75.93%. These percentages quantify the excess omitted by adding standalone damages, rather than the contribution of a single factor or the fraction attributable to warming.

Table 6 Standalone and interaction components of residential damage (billion JPY).

Climate	SLR	Standalone sum	Pairwise sum	Pure third-order term	Combined damage	Net non-additive damage	Share (%)
PGW2k	Lower	213.71	501.42	-5.75	709.38	495.67	69.87
	Central	216.80	578.77	-20.15	775.42	558.62	72.04
	Upper	232.34	704.20	-45.18	891.36	659.02	73.93
PGW4k	Lower	239.40	698.73	-40.62	897.50	658.11	73.33
	Central	254.19	793.28	-54.23	993.24	739.05	74.41
	Upper	284.02	955.96	-60.19	1179.79	895.77	75.93

Figure 9 shows pairwise and pure third-order terms calculated with Eq. (10). All pairwise terms were positive, while the third-order terms were negative. At central PGW4k SLR, the pairwise sum of 793.28 billion JPY exceeded the net non-additive damage. The third-order term of −54.23 billion JPY reconciled that difference. The negative sign indicates that the standalone and pairwise terms together exceed the fully combined response. It does not imply that adding a factor reduces total damage. PGW2k had the same positive-negative structure, with non-additive shares of 69.87-73.93%. At lower PGW2k SLR, the third-order term was only approximately 0.81% of total damage in absolute magnitude, leaving pairwise terms to explain most of the excess. Thus, the third-order term is needed for an exact reconstruction, but its magnitude is not uniformly large across scenarios. The decomposition resolves how positive pairwise effects and the remaining joint response combine to produce total damage.

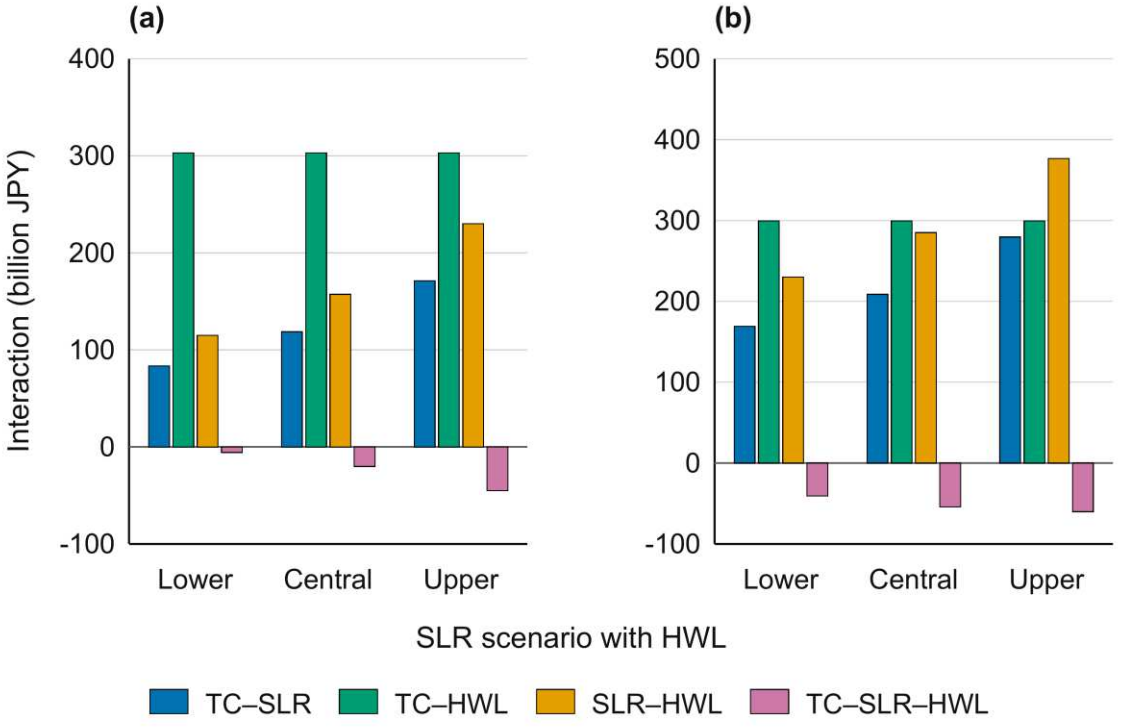

Fig. 9 Non-additive residential damage from pairwise and three-factor interactions in (a) PGW2k and (b) PGW4k. Vertical scales differ between panels.

Cellwise decomposition clarifies the negative domain total. At central PGW4k SLR, positive third-order terms summed to 200.77 billion JPY and negative terms to −255.00 billion JPY, yielding −54.23 billion JPY in **Fig. 9(b)**. Several combinations can inundate the same location, and added depth can either cross a damage threshold or remain within a class. Opposing local responses consequently cancel when aggregated. Cells already at the maximum damage ratio under a two-factor combination contributed less than 0.1% of the gross negative sum. Saturation at the upper damage limit therefore does not provide the primary explanation for the negative third-order term.

Grouping SLR and HWL into one background water level factor changed the central PGW4k non-additive share from 74.41% to 45.71% (**Supplementary Table S3**). Total damage remains 993.24 billion JPY in both calculations. Grouping transfers the SLR-HWL interaction of 285.06 billion JPY from the non-additive component into the standalone background response, leaving 453.99 billion JPY associated with combining TC and the background water level. The lower percentage therefore reflects a change in the reference used to define non-additivity, rather than a reduction in simulated damage. From lower to upper PGW4k SLR, the two-factor share declined from 47.70% to 43.99%, although its magnitude increased from 428.11 to 519.00 billion JPY. PGW2k shares ranged from 48.13% to 53.66%. Factor definitions thus affect the magnitude and SLR dependence of the share, but both definitions retain substantial excess damage from combining TC with elevated background water levels. The grouped comparison is especially useful here because SLR and HWL both enter the model as background-level increments. It checks whether the main conclusion depends on treating those increments as separate factors.

Such excess responses are relevant to compound hazard assessment [24]. The assessed drivers raise water surfaces relative to terrain and defense crests, while deeper inundation can cross damage thresholds. Non-additivity therefore includes hydrodynamic and damage-function effects. At central PGW4k SLR, non-additive shares were 33.80% for area, 75.30% for the maximum-depth-based volume metric, and 74.41% for damage. The larger volume-metric share shows that the

combined response extends beyond expansion of the inundation boundary. Its similarity to the damage share indicates that vulnerability alone does not explain the large excess, although this comparison does not independently separate the two effects.

For coastal adaptation assessment, these results support evaluating SLR jointly with storm forcing and high water conditions. Standalone damage sums miss a substantial part of the combined response. Relative shares should also be accompanied by absolute contributions, because a declining percentage can conceal increasing damage. Finally, additional losses within already inundated areas show why assessments need depth information alongside hazard boundaries. Together, these measures describe the magnitude, allocation, and spatial development of potential damage under the specified scenarios. They can inform subsequent comparisons of protective measures, whose effectiveness and costs were not evaluated here.

5 Conclusions

This study linked Faxai-based WRF ensemble mean atmospheric fields with JAGURS-surge to assess inundation and potential direct residential damage in Tokyo Bay under different climates, SLR projections, and prescribed high-water levels. Analysis of all factor combinations led to the following findings.

1. Approximately 73-76% of total PGW4k damage exceeded the sum of the three standalone damages. A non-additive share of approximately 44-48% remained when SLR and HWL were grouped, indicating that combined damage could not be described adequately by simply adding individual assessments.

2. The SLR share of PGW4k damage increased from 23.43% at lower SLR to 31.96% at upper SLR. TC and HWL declined in relative share but increased in absolute contribution, demonstrating the need to compare both allocation and magnitude.

3. Under the selected mean atmospheric fields at present-day MSL, PGW2k and PGW4k inundated areas were 47.3% and 57.5% larger than CTL, while residential damage increased by 89.9% and 104.4%. Damage increased faster than area, requiring inundation extent and depth-dependent damage ratios to be considered together.

4. With HWL fixed, intensification in previously inundated areas accounted for approximately 86-88% of the damage increase from lower to upper SLR in the two future climates. The PGW4k damage share from ground-referenced depths of at least 2.45 m also increased from 9.4% to 25.5%.

These experiments show how SLR alters potential damage under combined storm and high water conditions in Tokyo Bay. Established attribution and interaction methods distinguish the SLR contribution to total damage from the net excess above standalone responses. Their joint application provides a quantitative basis for evaluating sea-level impacts within compound coastal inundation

assessments. The spatial partition of additional damage further identifies depth increases within the existing inundation footprint that would be missed by considering changes in area alone.

The findings are conditional on the selected Faxai mean fields, static HWL, and uniform residential exposure. Evaluation across additional typhoons and individual members would clarify sensitivity to storm tracks and mean-field construction. Incorporating time-varying tides and actual building distributions would support comparisons of adaptation measures under more detailed hazard and exposure conditions.

Author contributions

Junbeom Jo: Data curation, Formal analysis, Methodology, Validation, Visualization, Writing - original draft. **Nobuhito Mori**: Resources, Conceptualization, Funding acquisition, Investigation, Methodology, Project administration, Supervision, Writing - review and editing.

Funding

This research was supported by research funds for newly appointed professors of Jeonbuk National University in 2026; the Moonshot Research and Development Program by Japan Science and Technology Agency (JST) [grant number JPMJMS2282].

Competing interests

The authors declare that they have no known competing financial interests or personal relationships that could have appeared to influence the work reported in this paper.

Data availability

The simulation outputs supporting the findings of this study are available from the corresponding author upon reasonable request. The sources of the input data are identified in the methods and reference list.

References

1. Nicholls, R. J. & Cazenave, A. Sea-level rise and its impact on coastal zones. Science 328, 1517–1520 (2010). https://doi.org/10.1126/science.1185782

2. Knutson, T. et al. Tropical cyclones and climate change assessment: Part II: Projected response to anthropogenic warming. Bull. Am. Meteorol. Soc. 101, E303–E322 (2020). https://doi.org/10.1175/BAMS-D-18-0194.1

3. Needham, H. F., Keim, B. D. & Sathiaraj, D. A review of tropical cyclone-generated storm surges: Global data sources, observations, and impacts. Rev. Geophys. 53, 545–591 (2015). https://doi.org/10.1002/2014RG000477

4. Muis, S., Verlaan, M., Winsemius, H. C., Aerts, J. C. J. H. & Ward, P. J. A global reanalysis of storm surges and extreme sea levels. Nat. Commun. 7, 11969 (2016). https://doi.org/10.1038/ncomms11969

5. Vousdoukas, M. I. et al. Global probabilistic projections of extreme sea levels show intensification of coastal flood hazard. Nat. Commun. 9, 2360 (2018). https://doi.org/10.1038/s41467-018-04692-w

6. Tebaldi, C. et al. Extreme sea levels at different global warming levels. Nat. Clim. Chang. 11, 746–751 (2021). https://doi.org/10.1038/s41558-021-01127-1

7. Sandi, C., Miyashita, T., Shimura, T. & Mori, N. Assessment of future nonstationary changes in extreme sea levels considering climate change for Southeast Asia using high-resolution climate forcing. Earth's Future 14, e2025EF007530 (2026). https://doi.org/10.1029/2025EF007530

8. Resio, D. T. & Irish, J. L. Tropical cyclone storm surge risk. Curr. Clim. Change Rep. 1, 74–84 (2015). https://doi.org/10.1007/s40641-015-0011-9

9. Bilskie, M. V., Hagen, S. C., Medeiros, S. C. & Passeri, D. L. Dynamics of sea level rise and coastal flooding on a changing landscape. Geophys. Res. Lett. 41, 927–934 (2014). https://doi.org/10.1002/2013GL058759

654 10. Arns, A. et al. Sea-level rise induced amplification of coastal protection design heights. Sci. Rep.
655 7, 40171 (2017). https://doi.org/10.1038/srep40171
656 11. Ke, Q. et al. An integrated framework of coastal flood modelling under the failures of sea dikes: a
657 case study in Shanghai. Nat. Hazards 109, 671–703 (2021). https://doi.org/10.1007/s11069-021-
658 04853-z
659 12. Horsburgh, K. J. & Wilson, C. Tide-surge interaction and its role in the distribution of surge
660 residuals in the North Sea. J. Geophys. Res. 112, C08003 (2007).
661 https://doi.org/10.1029/2006JC004033
662 13. Jo, J., Araki, Y., Baba, T., Kim, S. & Mori, N. Numerical study on tide-surge interaction and
663 sequential surge oscillations in Tokyo Bay. Ocean Eng. 357, 125439 (2026a).
664 https://doi.org/10.1016/j.oceaneng.2026.125439
665 14. Pickering, M. D. et al. The impact of future sea-level rise on the global tides. Cont. Shelf Res.
666 142, 50–68 (2017). https://doi.org/10.1016/j.csr.2017.02.004
667 15. Schär, C., Frei, C., Lüthi, D. & Davies, H. C. Surrogate climate-change scenarios for regional
668 climate models. Geophys. Res. Lett. 23, 669–672 (1996). https://doi.org/10.1029/96GL00265
669 16. Lackmann, G. M. Hurricane Sandy before 1900 and after 2100. Bull. Am. Meteorol. Soc. 96,
670 547–560 (2015). https://doi.org/10.1175/BAMS-D-14-00123.1
671 17. Mizuta, R. et al. Over 5,000 years of ensemble future climate simulations by 60-km global and
672 20-km regional atmospheric models. Bull. Am. Meteorol. Soc. 98, 1383–1398 (2017).
673 https://doi.org/10.1175/BAMS-D-16-0099.1
674 18. Fujita, M. et al. Precipitation changes in a climate with 2-K surface warming from large
675 ensemble simulations using 60-km global and 20-km regional atmospheric models. Geophys.
676 Res. Lett. 46, 435–442 (2019). https://doi.org/10.1029/2018GL079885

19. Fujiwara, K., Takemi, T. & Mori, N. Response of intensity and structure of Typhoon Jebi (2018) before landfall to 2-K and 4-K warmed future climates in dynamical downscaling experiments. SOLA 19, 142–149 (2023). https://doi.org/10.2151/sola.2023-019

20. Fujiwara, K., Takemi, T. & Mori, N. Impact of historical and future warming on heavy rainfall over eastern Japan induced by Typhoon Hagibis (2019) in dynamical downscaling simulations. Nat. Hazards 121, 1819–1832 (2025). https://doi.org/10.1007/s11069-024-06875-9

21. Li, Z. et al. Future changes in intense tropical cyclone hazards in the Pearl River Delta region: an air-wave-ocean coupled model study. Nat. Hazards 120, 7139–7154 (2024). https://doi.org/10.1007/s11069-024-06510-7

22. Wahl, T., Jain, S., Bender, J., Meyers, S. D. & Luther, M. E. Increasing risk of compound flooding from storm surge and rainfall for major US cities. Nat. Clim. Chang. 5, 1093–1097 (2015). https://doi.org/10.1038/nclimate2736

23. Bevacqua, E. et al. Higher probability of compound flooding from precipitation and storm surge in Europe under anthropogenic climate change. Sci. Adv. 5, eaaw5531 (2019). https://doi.org/10.1126/sciadv.aaw5531

24. Zscheischler, J. et al. Future climate risk from compound events. Nat. Clim. Chang. 8, 469–477 (2018). https://doi.org/10.1038/s41558-018-0156-3

25. Bennett, W. G. et al. Modelling compound flooding: a case study from Jakarta, Indonesia. Nat. Hazards 118, 277–305 (2023). https://doi.org/10.1007/s11069-023-06001-1

26. Toyoda, M., Mori, N., Kim, S., Shibutani, Y. & Yoshino, J. Assessment of compound occurrence of storm surge and river flood in Ise and Mikawa Bays, Japan using a framework of atmosphere-ocean-river coupling. Nat. Hazards 120, 3891–3917 (2024). https://doi.org/10.1007/s11069-023-06362-7

27. Jo, J., Kim, S., Kim, J. & Mori, N. Coastal and pluvial compound flooding of surge, wave, tide, rainfall-runoff, sewer flow, and seawall failure at coastal urban areas. J. Hydrol. 661, 133698 (2025). https://doi.org/10.1016/j.jhydrol.2025.133698

28. Yamamoto, K. et al. Compound flood simulations indicate rising public exposure to sewage-contaminated waters in Waikīkī, Hawai‘i. Sci. Rep. 16, 9740 (2026). https://doi.org/10.1038/s41598-026-38225-z

29. Hallegatte, S., Green, C., Nicholls, R. J. & Corfee-Morlot, J. Future flood losses in major coastal cities. Nat. Clim. Chang. 3, 802–806 (2013). https://doi.org/10.1038/nclimate1979

30. Hinkel, J. et al. Coastal flood damage and adaptation costs under 21st century sea-level rise. Proc. Natl Acad. Sci. USA 111, 3292–3297 (2014). https://doi.org/10.1073/pnas.1222469111

31. Kwak, C., Jo, J., Han, J., Kim, J. & Lee, S. Analysis of flood risk in Ulsan Metropolitan City, South Korea, considering urban development and changes in weather factors. Water 17, 2800 (2025). https://doi.org/10.3390/w17192800

32. Merz, B., Kreibich, H., Schwarze, R. & Thieken, A. H. Review article “Assessment of economic flood damage”. Nat. Hazards Earth Syst. Sci. 10, 1697–1724 (2010). https://doi.org/10.5194/nhess-10-1697-2010

33. Huizinga, J., de Moel, H. & Szewczyk, W. Global flood depth-damage functions: Methodology and the database with guidelines. EUR 28552 EN (Publications Office of the European Union, Luxembourg, 2017). https://doi.org/10.2760/16510

34. Li, Y., Wang, L., Li, F., Peng, S. G. & Ding, C. Quantitative estimation of urban flood damage from storm surges for a coastal city. Nat. Hazards 121, 16915–16934 (2025). https://doi.org/10.1007/s11069-025-07456-0

35. Li, X., Yoshimura, K. & Fudeyasu, H. Impact-based flood-damage assessment in Japan under longitudinal typhoon-track perturbations and levee-height variations during Hagibis (2019). Commun. Earth Environ. 7, 787 (2026). https://doi.org/10.1038/s43247-026-04077-8

36. Chaigneau, A. A., Toimil, A., Alvarez-Cuesta, M. & Menéndez, M. Escalating coastal flood risk and impact thresholds in Miami revealed by Hurricane Irma. Sci. Rep. https://doi.org/10.1038/s41598-026-64891-0 (2026).

37. Jo, J., Mori, N. & Araki, Y. Cascading amplification from typhoon-intensity perturbations to potential surge-induced residential damage in Tokyo Bay. Coast. Eng. J. (manuscript under review, 2026b).

38. Shapley, L. S. A value for n-person games. In Contributions to the Theory of Games Vol. II (eds Kuhn, H. W. & Tucker, A. W.) 307–318 (Princeton University Press, Princeton, 1953). https://doi.org/10.1515/9781400881970-018

39. Chowdhury, M. E., Lee, J.-W. & Lee, W. Spatiotemporal quantification of relative contributions of compound flood drivers using Shapley value-based approach. J. Hydrol. 677, 135808 (2026). https://doi.org/10.1016/j.jhydrol.2026.135808

40. Harsanyi, J. C. A simplified bargaining model for the n-person cooperative game. Int. Econ. Rev. 4, 194–220 (1963). https://doi.org/10.2307/2525487

41. Skamarock, W. C. et al. A description of the Advanced Research WRF Version 3. NCAR Technical Note NCAR/TN-475+STR (2008). https://doi.org/10.5065/D68S4MVH

42. Baba, T. et al. Parallel implementation of dispersive tsunami wave modeling with a nesting algorithm for the 2011 Tohoku tsunami. Pure Appl. Geophys. 172, 3455–3472 (2015). https://doi.org/10.1007/s00024-015-1049-2

43. Honda, T. & Mitsuyasu, H. Experimental study of wind stress in the sea surface. Proc. Jpn. Conf. Coast. Eng. 27, 90–93 (1980) (in Japanese).

44. Homma, M. Discharge coefficient on overflow weir (part-2). JSCE Magazine, Civil Engineering 26, 849–862 (1940) (in Japanese).

45. MLIT. Guidelines for cost-benefit analysis of Japan Coastal Projects (Ministry of Land, Infrastructure, Transport and Tourism, Japan, 2024) (in Japanese).

750 46. Tokyo Metropolitan Government. Life and Statistics 2024: Tokyo in the national context (Bureau
751 of General Affairs, Tokyo Metropolitan Government, 2024) (in Japanese).
752 47. Tokyo Metropolitan Government. Households and population based on the Basic Resident
753 Register, 1 February 2025, Japanese and foreign residents.
754 https://www.toukei.metro.tokyo.lg.jp/juukim/jm-index.htm (2025) (in Japanese).
755 48. MEXT & JMA. Climate Change in Japan 2025: Assessment report on observations and
756 projections of the atmosphere, land and oceans. Detailed report (Ministry of Education, Culture,
757 Sports, Science and Technology and Japan Meteorological Agency, Japan, 2025) (in Japanese).
758 https://www.data.jma.go.jp/cpdinfo/ccj/2025/html_honpen/cc2025_honpen_index.html
759 49. Japan Meteorological Agency. RSMC Tokyo best-track data for Typhoon Faxai (1915), revision
760 dated 14 November 2019. https://www.jma.go.jp/jma/jma-eng/jma-center/rsmc-hp-pub-
761 eg/besttrack.html (2019b; accessed 13 October 2026).
762 50. Japan Meteorological Agency. Historical weather data: Tokyo station, 8-9 September 2019, 10-
763 minute observations. https://www.data.jma.go.jp/stats/etrn/index.php (2019a; accessed 13
764 October 2026).

Supplementary Files

This is a list of supplementary files associated with this preprint. Click to download.

- SupplementaryInformation.docx